ACS OMEGA

http://pubs.acs.org/journal/acsodf

Article

Enhancing the Areal Capacity and Stability of Cu_2ZnSnS_4 Anode Materials by Carbon Coating: Mechanistic and Structural Studies During Lithiation and Delithiation

Boya Venugopal, Zeru Syum, Sheng-Yu Yu, Amr sabbah, Indrajit Shown, Chih-Wei Chu, Li-Chyong Chen, Chih-Hao Lee,* Heng-Liang Wu,* and Kuei-Hsien Chen*

Cite This: *ACS Omega* 2022, 7, 9152−9163

Read Online

ACCESS | Metrics & More | Article Recommendations | Supporting Information

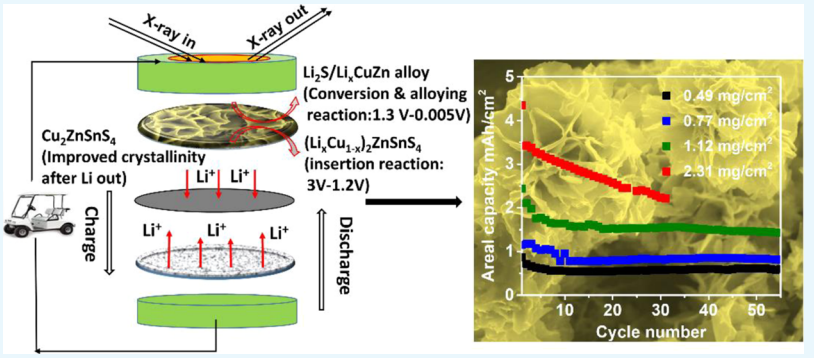

ABSTRACT: The widespread use of energy storage technologies has created a high demand for the development of novel anode materials in Li-ion batteries (LIBs) with high areal capacity and faster electron-transfer kinetics. In this work, carbon-coated Cu_2ZnSnS_4 with a hierarchical 3D structure (CZTS@C) is used as an anode material for LIBs. The CZTS@C microstructures with enhanced electrical conductivity and improved Li-ion diffusivity exhibit high areal and gravimetric capacities of 2.45 mA h/cm^2 and 1366 mA h/g, respectively. The areal capacity achieved in the present study is higher than that of previously reported CZTS-based materials. Moreover, *in situ* X-ray diffraction results show that lithium ions are stored in CZTS through the insertion reaction, followed by the alloying and conversion reactions at ∼1 V. The structural evolution of Li_2S and Cu−Sn/Cu−Zn alloy phases occurs during the conversion and alloying reactions. The present work provides a cost-effective and simple method to prepare bulk CZTS and highlights the conformal carbon coating over CZTS, which can enhance the electrical and ionic conductivities of CZTS materials and increase the mass loading (1−2.3 mg/cm^2). The improved stability and rate capability of CZTS@C anode materials can therefore be achieved.

INTRODUCTION

The increasing demand for electric vehicles and portable electronic devices has prompted new research into the development of Li-ion batteries (LIBs) with higher energy density. Although graphite anode materials have been widely used in LIBs, their low theoretical capacity (372 mA h/g) and poor rate capability limit their potential in the development of high-energy density LIBs.[1−3] Therefore, it is highly desirable to develop new anode materials for LIBs with high energy and power density, as well as good stability.[4] Various anode materials such as transition-metal oxides (Fe_2O_3 and SnO_2) and metals (Si and Sn) have been explored.[1,3,5,6] Among these materials, Si has received considerable attention because of its high gravimetric capacity and stability at low mass loadings. However, anode materials with high mass loading and high areal capacity are needed for practical applications. Although high mass loadings of the Si anode lead to significantly improved areal capacities (1−3.5 mA h/cm^2), the Si material suffers from the low Coulombic efficiency (CE) and large volume expansion of the active material, resulting in poor reversibility and fast capacity fading. On the other hand, materials with 2D-layered structures and large interlayer spacing, such as SnS_2 and MoS_2, improve the Li-ion diffusivity and suppress the volume expansion.[7−9] Unfortunately, these anode materials suffer from low conductivity and poor rate capability.[10]

Received: September 13, 2021
Accepted: February 2, 2022
Published: March 14, 2022

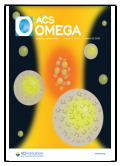

https://doi.org/10.1021/acsomega.1c05076
ACS Omega 2022, 7, 9152−9163

Scheme 1. Synthesis Process of CZTS@C

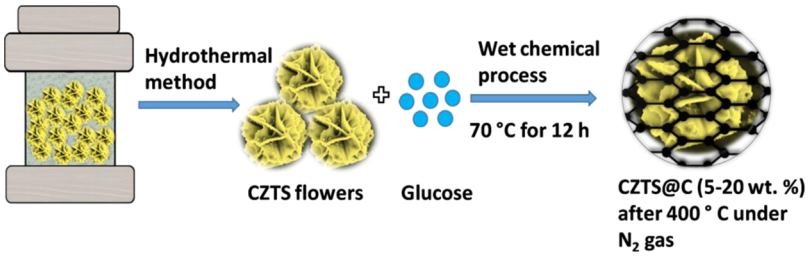

Recently, several research groups demonstrated the application of multimetallic (Cu, Zn, and Sn) sulfides, such as Cu_2SnS_3 and Cu_2ZnSnS_4 (CZTS), as anode materials for LIBs, wherein Sn and Zn can easily form alloys with lithium and provide high capacity.[11,12] The earth-abundant transition metals (e.g., Cu_2SnS_3 or CZTS) act as a buffer matrix, enabling alloying and conversion reactions that result in high capacity.[13] Moreover, discharge products such as the Cu−Zn alloy formed during lithiation can also enhance the conductivity of the electrode during cycling.[14] Thus, CZTS has been regarded as the advanced anode material with enhanced energy and power densities in next-generation LIBs. Yang *et al.* demonstrated the first CZTS-based anode for LIBs with initial discharge and charge capacities of 857 and 288 mA h/g, respectively.[15] This system maintained a capacity around 234 mA h/g after 30 cycles, and it exhibited a low initial CE and poor electrochemical performance. Later, Jiang *et al.* reported the electrochemical performance of CZTS nanoflowers with high capacity and stability at low current rates (100 mA/g).[16] Another study showed that CZTS thin films exhibited a high capacity of about 668 mA h/g at a current rate of 100 mA/g. However, the CZTS thin films exhibited a low areal capacity of ∼0.45 mA h/cm^2 with a limited mass loading of 0.5 mg/cm^2, and the material processing approach was also expensive.[17] Recently, Chiu et al. demonstrated that CZTS thin films exhibited high discharge capacity (1400 mA h/g) and stability over 400 cycles, but a low mass loading of 0.3 mg/cm^2 was obtained.[14] Bree *et al.* also reported that CZTS thin films with mass loadings of 0.1−0.2 mg/cm^2 delivered a stable discharge capacity of about 600 mA h/g at a current rate of 500 mA/g.[13] Although CZTS anode materials have shown promising electrochemical performance, they are far from satisfying the commercial requirements, mainly due to their low areal capacity (<0.5 mA h/cm^2) and limited mass loadings. In addition, the mechanistic studies of CZTS were rare.

In this work, we proposed a cost-effective and simple process to develop advanced CZTS anode materials with a bulk structure coated with different amounts of carbon (hereafter named CZTS@C) and high mass loadings. The CZTS@C material used as an anode in LIBs exhibits a high gravimetric capacity of 1366 mA h/g and areal capacities of 1−2.45 mA h/cm^2 upon cycling. The stability of CZTS@C is improved during cycling, which could result from the formation of a stable solid−electrolyte interphase (SEI). Electrochemical impedance spectroscopy (EIS) results show that the carbon coating improves the conductivities of CZTS anode materials during cycling. *In situ* X-ray diffraction (XRD) is employed to examine the reaction mechanism of the CZTS@C material. The formation of Li_2S at low potential and the evolution of various Cu−Sn/Cu−Zn alloys are obtained during the charge−discharge process, suggesting that multiple electron-transfer process results in a high theoretical capacity. The present study provides new insights into the use of quaternary sulfides as high-performance anode materials with higher energy density for the development of advanced LIBs.

RESULTS AND DISCUSSION

Morphology and Crystal Structure. The desired carbon content in the CZTS@C samples was controlled from 5 to 20 wt %, as determined by elemental analysis (EA). The CZTS@C samples with carbon contents of 4.4, 6.9, 9.7, 13.6, and 20.3 wt % are denoted as CZTS@C-5, CZTS@C-7, CZTS@C-10, CZTS@C-15, and CZTS@C-20, respectively (Supporting Information, Table S1). The synthesis process of CZTS@C is illustrated in Scheme 1. The field-emission scanning electron microscopy (FE-SEM) images of pristine CZTS show a 3D flower-like morphology composed of petal-like interconnected CZTS nanosheets with a thickness of few nanometers (Figure 1a). The FE-SEM images in Figure 1b−f show that the morphology of CZTS remains the same even after coating with different amounts of carbon, indicating that carbon could successfully encapsulate the CZTS nanosheets as a thin film. Even at higher carbon coatings (13.6 wt %, CZTS@C-15), the CZTS nanosheet surface was uniformly covered with a thin carbon layer, and no local agglomeration was observed. Previous studies suggest that the uniform carbon coating

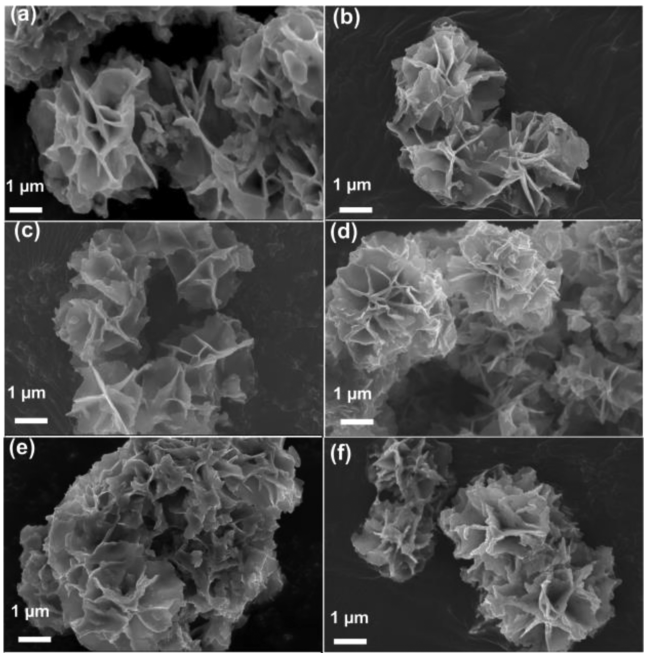

Figure 1. FE-SEM images of (a) CZTS, (b) CZTS@C-5, (c) CZTS@C-7, (d) CZTS@C-10, (e) CZTS@C-15, and (f) CZTS@C-20 samples.

https://doi.org/10.1021/acsomega.1c05076
ACS Omega 2022, 7, 9152−9163

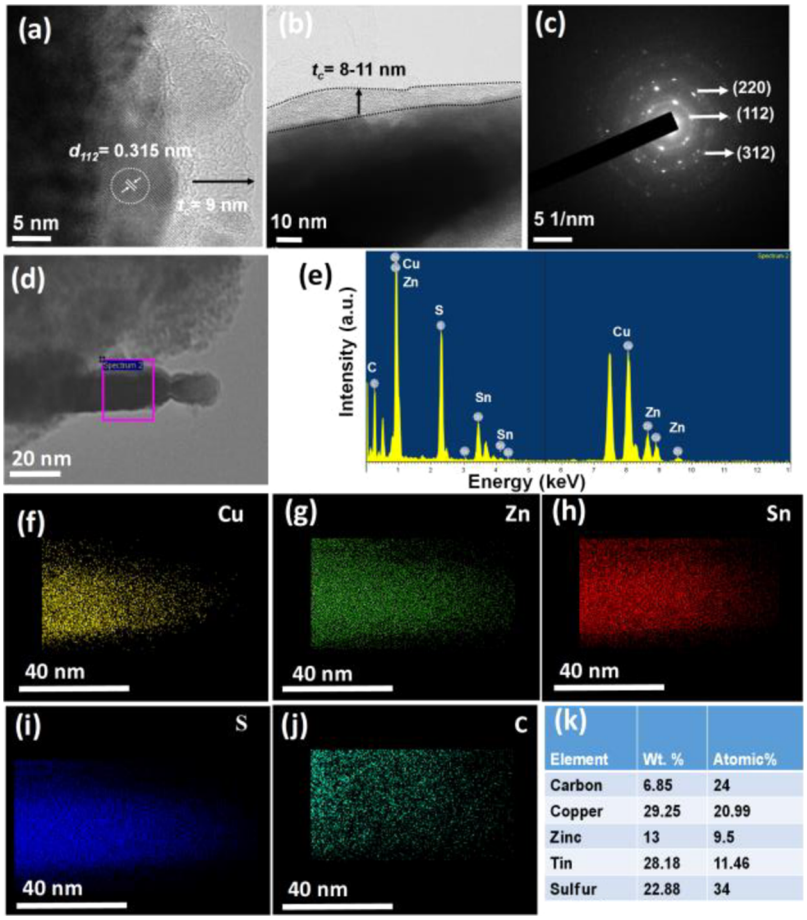

Figure 2. (a,b) HRTEM images, (c) SAED pattern, (d) HAADF image, (e) EDX elemental pattern (f–j), EDX elemental mappings, and (k) EDX file of Cu, Zn, Sn, S, and C elements in the CZTS@C-15 sample.

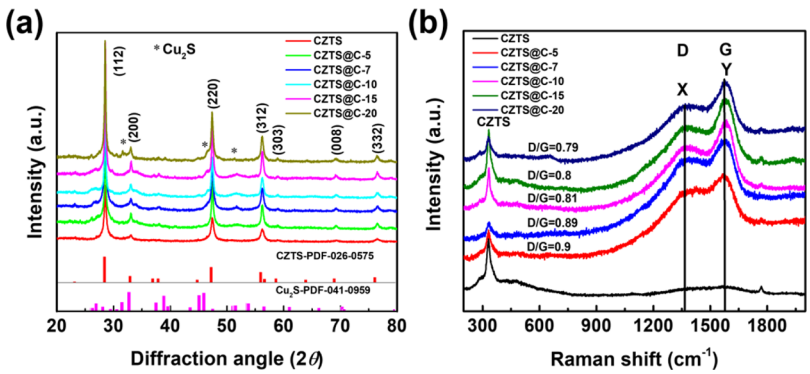

Figure 3. (a) XRD and (b) Raman spectra of CZTS and CZTS@C samples.

layer on the material avoids direct contact with the electrolyte and controls the SEI film thickness. The stability of the material can be improved.[18]

The morphology and microstructure of CZTS@C-15 were investigated using high-resolution transmission electron microscopy (HRTEM). Figure 2a,b shows that the CZTS surface was coated with amorphous carbon uniformly and the thickness of the carbon layer was ~10 nm. The lattice fringe with an interplanar spacing of 0.315 nm is consistent with the (112) *d*-spacing of kesterite CZTS (PDF no. 26-0575).[12,19] The selected-area electron diffraction (SAED) pattern of CZTS highlights the polycrystalline nature of the sample, and all diffraction rings are associated with the (112), (220), and (312) lattice planes of kesterite CZTS (Figure 2c).[12] Figure 2d–k shows the high-angle annular dark-field (HAADF) image and energy-dispersive X-ray spectroscopy (EDX) elemental pattern as well as the elemental mapping of CZTS@C-15. The elemental composition measurements of CZTS@C-15 show that the Cu, Zn, Sn, S, and C elements are evenly distributed within the 3D nanostructure of the sample.

We next employ XRD measurements to determine the crystal structure of the as-synthesized CZTS and CZTS@C samples (Figure 3a). The XRD peaks at 2θ = 28.5, 32.9, 47.3, and 56.4° are associated with the (112) (200), (220), and (312) lattice planes, respectively, which is consistent with previous studies (JCPDS no. 26-0575) (Figure S1).[19] In

https://doi.org/10.1021/acsomega.1c05076
ACS Omega 2022, 7, 9152−9163

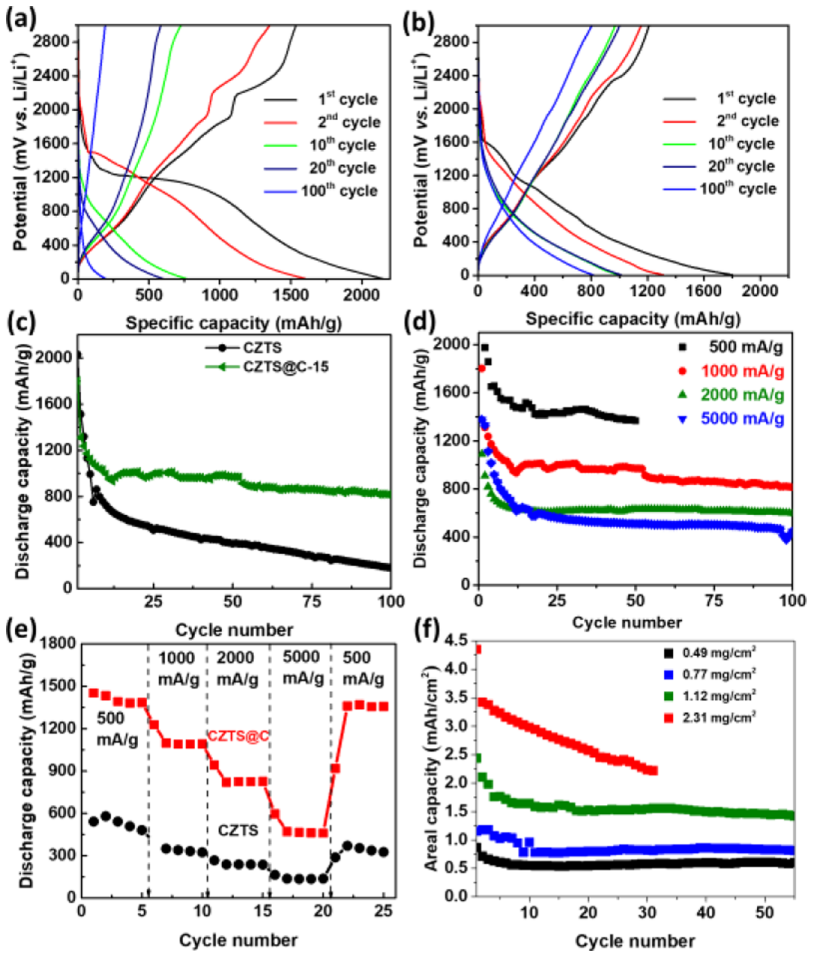

Figure 4. Electrochemical charge−discharge curves for (a) CZTS and (b) CZTS@C-15 with mass loading 1.1 mg/cm^2 at a current density of 1000 mA/g, from the first to 100th cycle; (c) cycling performance at a current density of 1000 mA/g of CZTS and CZTS@C samples with various carbon contents; (d) cycling performance of CZTS@C-15 at various current densities; (e) rate performances of CZTS and CZTS@C-15 from 500 to 5000 mA/g; and (f) areal capacity of CZTS@C-15 samples with various mass loadings at a current density of 0.5 mA/cm^2.

addition, the XRD of CZTS@C materials shows the peaks at 32.5 and 52.4°, which can be attributed to the formation of a secondary $Cu_{2-x}S$ phase upon the annealing process.[20−22] The XRD results of CZTS@C exhibit the sharper diffraction pattern with stronger intensity than that of pristine CZTS, suggesting that the grain size and crystallinity of CZTS are changed after the coating process. The calcination process was performed at 400 °C, which could further improve the crystallinity of CZTS. Also, the coating process could result in the larger grain size of CZTS (Table S2).

Raman spectroscopy was used to study the phase of carbon-coated CZTS. Figure 3b shows the Raman spectra of the CZTS-based materials. The peaks at 287−288 and 335 cm^{-1} are associated with kesterite CZTS.[21,22] Moreover, the Raman peaks at 1355 and 1585 cm^{-1} are assigned to the D- and G bands originating from carbon, respectively.[23] Herein, the intensity of D/G ratio is 0.9 for CZTS@C with the carbon content below 10 wt % and 0.8 for CZTS@C with a carbon content above 10 wt %, respectively. The D/G ratio of the CZTS@C samples is close, suggesting that the degree of graphitization is similar in different carbon contents. In addition, the peak with weak intensity at ∼1750 cm^{-1} is assigned to the M band, which is an overtone of the out-of-plane phonon and has been observed in graphite and single-walled nanotube samples.[24,25]

Electrochemical Behavior of As-Prepared Electrodes.

Figure 4a,b shows the charge/discharge voltage profiles of the CZTS and CZTS@C-15 materials in different cycles at a current density of 1000 mA/g. The discharge profile of CZTS shows a broad discharge plateau at ∼1 V in the first discharge process and is attributed to the SEI layer formation with Li_2S as one of the main products. In contrast, this broad discharge plateau diminishes remarkably with the controlled SEI layer, mainly due to the carbon coating (see Figure 4b). The subsequent plateaus located below 1 V could be attributed to the generation of Li_xZn and Li_xSn alloys and Li_2S in both CZTS and CZTS@C materials. After 100 cycles, the charge−discharge curve of CZTS exhibits no plateaus, which results from the severe volume expansion during lithiation and delithiation processes. The volume expansion also results in poor electrical and ionic pathways during cycling. In contrast, the CZTS@C material exhibits better stability over cycling. A similar kind of information is obtained in other carbon-coated CZTS materials (please see Figure S2). Figure S3 shows that the CZTS-based materials with different carbon coating amounts exhibited different performances, suggesting that the performance of CZTS can be optimized by adjusting the carbon coating level.

Figure 4c shows that the electrochemical performance of the both CZTS and CZTS@C-15 material with a mass loading of

https://doi.org/10.1021/acsomega.1c05076
ACS Omega 2022, 7, 9152−9163

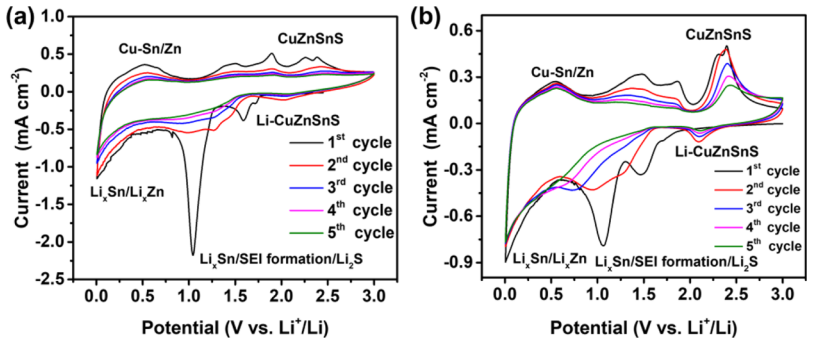

Figure 5. CV curves of (a) CZTS and (b) CZTS@C-15 materials cycled at a potential sweep rate of 0.2 mV s^{-1} in the potential range ranging from 0.005 to 3 V.

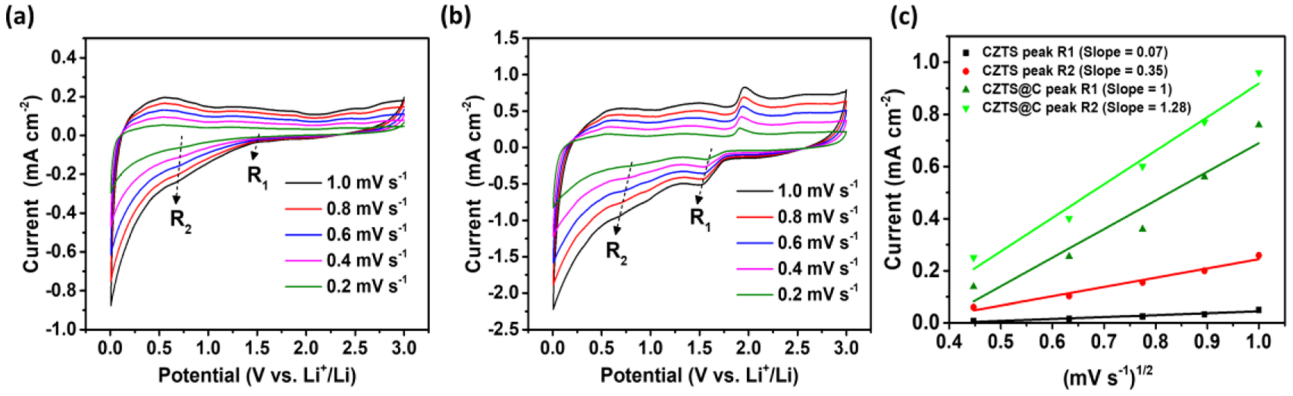

Figure 6. CV curves of (a) CZTS and (b) CZTS@C-15 after 100 cycles at different potential sweep rates; (c) linear relationship between the anodic peak current (i_p) and square root of scan rate ($v^{1/2}$) of CZTS and CZTS@C-15 after 100 cycles.

1.1 mg/cm^2. The CZTS material exhibits a discharge capacity of 2148 mA h/g in the initial cycle and the capacity fades drastically during cycling. The CZTS@C-15 shows a discharge capacity of 1802 mA h/g in the first cycle and reaches a discharge capacity of 815 mA h/g after 100 cycles, which represents the best performance among the CZTS-based materials. Although the initial discharge capacity of CZTS varies with different carbon contents, the initial discharge capacity of CZTS is 1200−1600 mA h/g when the carbon content is ranging from 0 to 15%. The CZTS@C-15 exhibits better electrochemical stability and the poor electrochemical performance of CZTS@C-20 is obtained. Moreover, CZTS-based materials exhibit an initial CE nearly 70% and increase to 100% in the following cycles (Figure S4). The low CE suggests that an irreversible reaction and side reaction, such as the formation of SEI, take place in the initial cycles.[26]

The thin carbon coating layer on the CZTS@C-15 could act as a buffer layer to prevent the aggregation of CZTS particles during cycling and thus mitigate the pulverization problems. As compared to other CZTS materials with a carbon content below 10%,[27] CZTS could be fully covered by 15% carbon and exhibits the better electrochemical performance. Upon a further increase of the carbon content (~20 wt %), the CZTS@C-20 gives a lower initial capacity, which could result from the excess carbon on the CZTS.

Figure 4d shows that CZTS@C-15 cycled at current densities of 500, 1000, 2000, and 5000 mA/g exhibits the capacities of 1366 (after 50 cycles), 815, 600, and 447 mA h/g after 100 cycles. CZTS@C-15 shows a capacity of ~220 mA h/g after 450 cycles at a high current rate of 5000 mA/g (Figure S5). Figure 4e shows the performance rate capability tests of CZTS and CZTS@C-15 from 500 to 5000 mA/g. CZTS@C-15 exhibits high discharge capacities of 1385, 1080, 825, and 460 mA h/g at current densities of 500, 1000, 2000, and 5000 mA/g, respectively. CZTS@C-15 also shows good reversibility cycled at different current densities. Moreover, we compare the cycling performance and mass loading of CZTS@C materials with other CZTS-based materials reported in the literature (Table S3). CZTS materials with different structures have been investigated in LIBs.[12−14,17,] However, the mass loading (0.2−0.3 mg/cm^2) and areal capacity (0.2−0.5 mA h/cm^2) of these anode materials are insufficient to meet the requirements of advanced LIBs. Thus, the cycling performance and the stability of CZTS@C materials with high mass loading obtained at high current rates should be taken into consideration. Figure 4f shows that CZTS@C-15 with mass loadings of 0.49, 0.77, 1.12, and 2.31 mg/cm^2 exhibits areal capacities of 0.61, 0.83, 1.45, and 2.45 mA h/cm^2 at a current density of 0.5 mA/cm^2, respectively, suggesting that large areal capacity and higher mass loading of CZTS@C-15 can be achieved. The battery performance obtained at various current rates is promising in the comparison of those reported silicon and germanium anodes.[28−30] The CZTS@C-15 anode material is also examined in the full cell with a NMC532 cathode at a current density of 100 mA/g in the potential window ranging from 1.5 to 4.5 V (Figure S6).

To investigate the electrochemical behavior of CZTS-based materials, Figure 5a,b shows cyclic voltammetry (CV) measurements of the CZTS and CZTS@C electrodes during five cycles. The potential window is between 0.005 and 3 V and the scan rate is 0.2 mV s^{-1}. The CV of the CZTS material shows two reduction peaks at ~1.5 and ~1 V in the first cycle

https://doi.org/10.1021/acsomega.1c05076
ACS Omega 2022, 7, 9152−9163

(Figure 5a). The reduction peak around 1.5 V can be attributed to lithium insertion in CZTS to form a partial Li_xCZTS phase, while the peak at 1.04 V may be related to the further conversion of Li_xCZTS, which results in the formation of Li_2S, Li_xSn alloys as well as the SEI layer, as previously reported.[11,12,31,32]

XRD results of CZTS and CZTS@C-15 show that the CZTS has a smaller particle size (Figure 3a). The current density of reduction peak at 1.04 V in CZTS is higher than that of in CZTS@C-15 at the first cycle, which could result from the higher surface area of CZTS. The CZTS material with a higher surface area offers more reaction sites for more lithium-ion storage, which is consistent with electrochemical behavior of CZTS and CZTS@C-15 during the first cycle (Figure 4a,b). The broad peak around 0.7 V could be associated with the Li insertion process in various alloys such as Cu−Sn/Zn and Li_2S. The delithiation process of CZTS shows four oxidation peaks at 0.5, 1.45, 1.9, and 2.3−2.4 V, which are associated with conversion and delithiation processes.[33−35] The following cycles show similar redox features, suggesting that the electrochemical behavior of CZTS becomes stable. The redox features with larger current density in the first cycle could result from the irreversible reactions.[36] The CV curves of CZTS@C and CZTS show similar features, suggesting that reaction behavior of CZTS could be similar to the CZTS@C and carbon coating has less contribution in the redox reactions.

We next examine the Li^+-ion diffusion kinetics of CZTS and CZTS@C-15. Figure 6a,b shows CV curves of CZTS and CZTS@C-15 after 100 cycles at different potential sweep rates. The relationship between the square root of the scan rate ($v^{1/2}$) and the anodic peak current (i_p) is illustrated in Figure 6c. The linear relationship and corresponding slope of the i_p *versus* $v^{1/2}$ plots provide insights into the charge storage kinetic behavior. In particular, the Randles−Sevcik equation can be used to analyze the Li^+-ion diffusion kinetics in CZTS anode materials[37]

$$i_p = (2.69 \times 10^5) n^{3/2} \times S \times D^{1/2} \times C \times v^{1/2} \quad (1)$$

In equation 1, n is the electron-transfer number, S is the electrode area (cm^2), i_p is the anodic peak current, D is the diffusion coefficient of Li^+, C is the bulk concentration of Li^+ in the electrode, and v is the scan rate. The electrode area and bulk concentration used in this study are 0.945 cm^2 and 1, respectively. Based on the current density of reduction peaks (R1 and R2), the slope obtained for the CZTS@C-15 anodic current is higher than that of CZTS, indicating that CZTS@C has a higher lithium-ion diffusion coefficient and faster electrochemical kinetics.

The electrochemical tests show that carbon-coated CZTS with high areal capacity exhibits a promising performance. To further understand the stability of the CZTS material, the morphologies of CZTS and CZTS@C-15 after 100 cycles were analyzed by FE-SEM (Figure S7). The morphology of CZTS changes substantially after 100 cycles and the morphology of carbon-coated CZTS shows less changes after cycling.

Electrochemical Reaction Mechanism. In order to study the reaction mechanism of CZTS@C-15 during the reversible cycles, *in situ* XRD experiments were conducted for the cycled CZTS@C-15 material. Figure 7 shows the *in situ* XRD patterns of CZTS@C-15, which exhibits an obvious peak shift and undergoes phase decomposition during the charge−discharge process. A variety of species, such as Li_2S and Cu−Zn/Cu−Sn

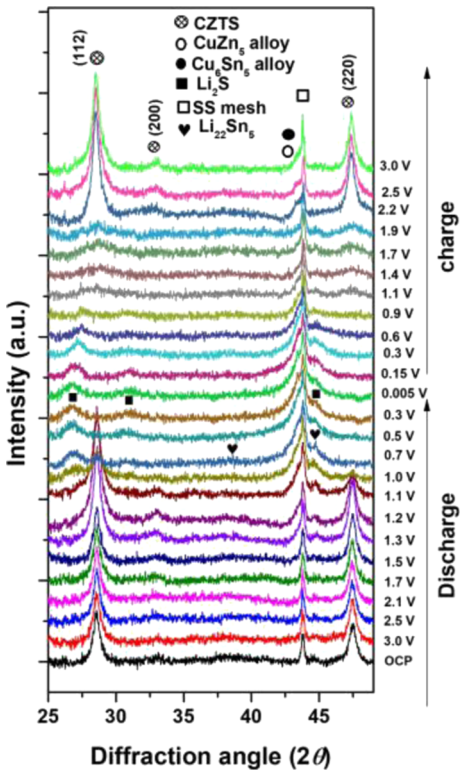

Figure 7. *In situ* XRD spectra of the CZTS@C-15 sample during the discharge−charge process between 0.005 and 3 V.

alloy phases, is formed at ∼1 V during the lithiation process and the CZTS-associated peak completely disappears at the end of the insertion process. During the delithiation process, *in situ* XRD results show that Li_2S and Cu−Zn/Cu−Sn alloys are converted to CZTS. Interestingly, the crystallinity of CZTS is improved after cycling. The residual metal alloys remain after cycling, which correspond to the irreversible reaction during the initial cycles.[38]

Formation of Li_2S and Cu−Zn/Cu−Sn Metal Alloys. The reaction mechanism of CZTS@C can be divided into four regions. Figure 8 shows the representative *in situ* XRD patterns of CZTS@C taken from Figure 7. First, the early stage at ∼2.1 and ∼1.5 V is attributed to the electrochemical activation of CZTS@C during the lithiation process. The main diffraction peak corresponding to the (112) plane slowly shifted from 28.54 to 28.49° degree during the lithiation process (3.0 V-2.1 V), reflecting the volume expansion of CZTS as well as the increase in lattice parameters. Thus, the insertion process is obtained above ∼1.3 V. Interestingly, the (112) diffraction peak became more intense and shifted toward higher angles below 1.3 V (Figure 8a,b). This unexpected behavior is due to Li^+ ions with a larger covalent radius (1.33 Å) replacing smaller copper ions (1.27 Å) in CZTS.[39,40] A higher bond distance for Li−S (2.45 Å) compared to Cu−S (2.37 Å) is obtained, which causes the increase in the lattice constant and particle size of CZTS from 3 to ∼1.2 V (Table S4). In addition, Figure 8c shows that the broad peaks at ∼43°are attributed to the formation of various metal alloys. *Ex-situ* XRD spectra of CZTS@C obtained at 1.05 V and 0.5 V during the lithiation process, suggesting that two broad peaks at ∼43° are attributed to the Cu−Sn/Cu−Zn metal alloys (Figures S1 and S8).

Second, the intensity of the characteristic CZTS@C peaks significantly decreases when CZTS@C is further lithiated ∼1

https://doi.org/10.1021/acsomega.1c05076
ACS Omega 2022, 7, 9152−9163

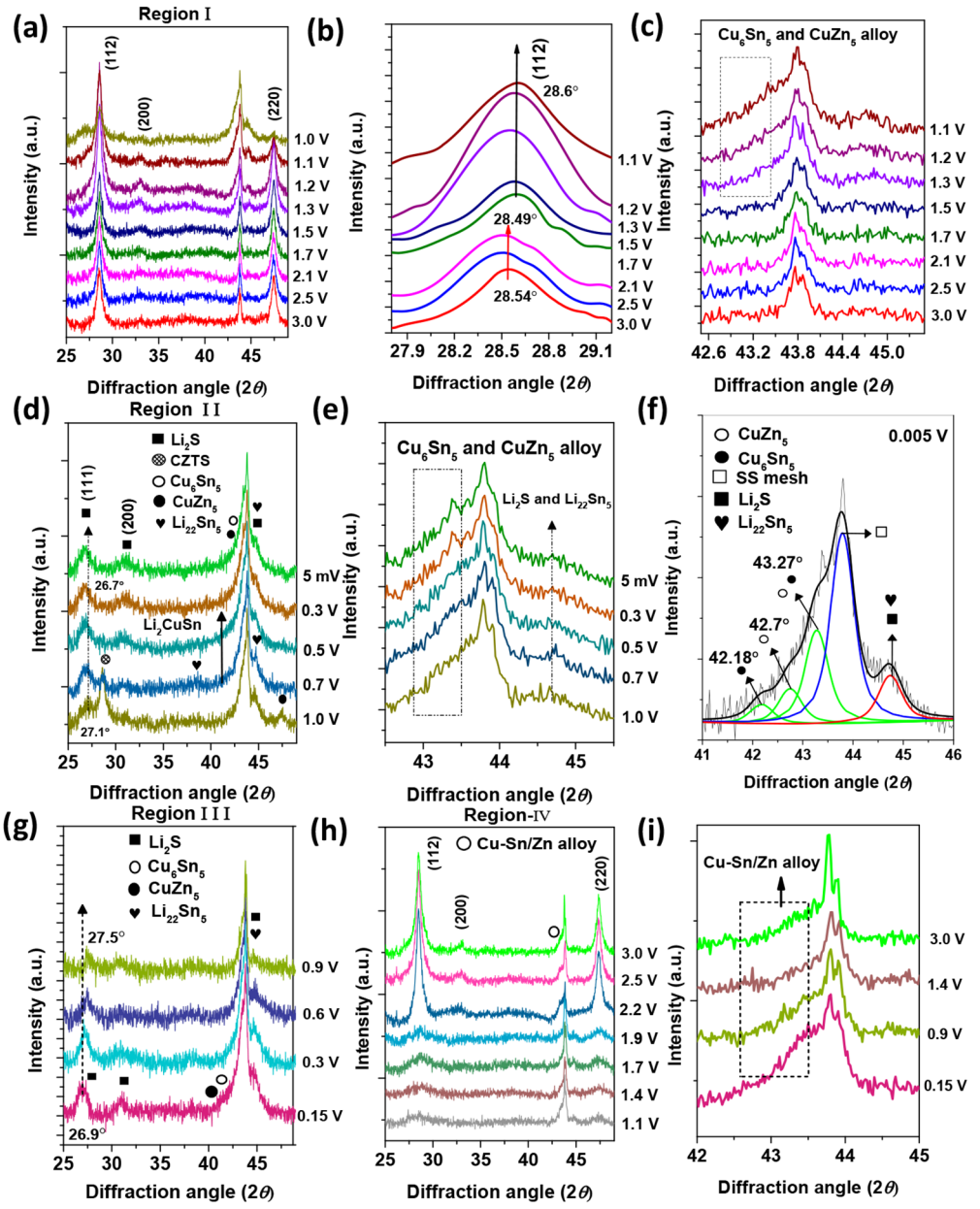

Figure 8. Representative *in situ* XRD results of the CZTS@C-15 taken from Figure 7 during the (a–f) lithiation (3–0.005 V) and (g–i) delithiation (0.005–3 V) processes.

V. Meanwhile, the peaks associated with the Li_2S phase appear at 27.1 and 31.1°, suggesting that a conversion reaction is taking place at the low potential region.[41] Also, the Li_2S phase with a face-centered cubic structure becomes more prominent. Figures 8d–f and S9 show the formation of Cu_6Sn_5 and $CuZn_5$ alloys during the discharge process. Cu_6Sn_5 and $CuZn_5$-associated peaks shift to lower angles, suggesting that the insertion process of Cu_6Sn_5 and $CuZn_5$ alloys is proceeded. At below 0.5 V, the (111) Li_2S-associated peak becomes broader. Thus, *in situ* XRD results suggest that CZTS can initially store lithium ions through insertion reactions followed by the formation of Cu–Sn/Cu–Zn metal alloys and Li_2S through the conversion process. During the conversion process, the insertion process of Cu–Sn/Cu–Zn metal alloys seems take place at lower potential region. Because the formation of $Li_{4.4}Sn$ has been proposed in the previous study,[12,42] some XRD peaks with weak intensity could be associated with the $Li_{22}Sn_5$ structure.

Reformation of CZTS during the Charge Process. Third, Figure 8g shows that the Li_2S-associated peak slowly shifts from lower angles (26.9°) to higher angles (27.4°) during the charge (delithiation) process from 0.15 to 0.9 V, indicating a volume contraction of Li_2S. Fourth, Figure 8h,i shows that Li_2S and the alloy-associated peaks disappear and CZTS is formed from 1.1 to 3 V, suggesting that the conversion and alloying reactions overlap upon cycling. The intensity of the CZTS peaks became stronger and sharper, suggesting that the CZTS with good crystallinity can be reformed during cycling.[14] In addition, in order to provide the insights into the reaction mechanism of CZTS@C after cycling, *ex situ* XRD measurement of CZTS@C was performed. The representative *ex situ* XRD results of CZTS@C-15 show the formation of the discharged species

https://doi.org/10.1021/acsomega.1c05076
ACS Omega 2022, 7, 9152–9163

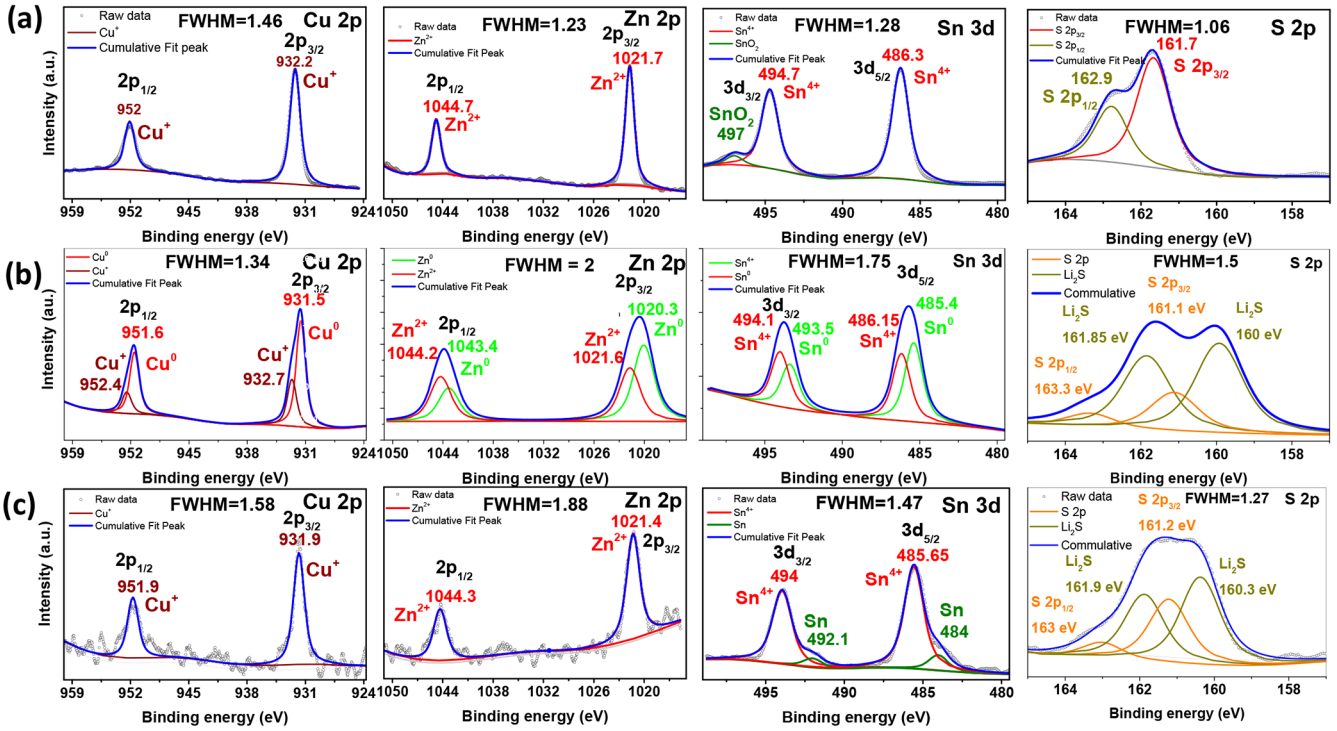

Figure 9. High-resolution Cu 2p, Zn 2p, Sn 3d, and S 2p XPS spectra of (a) pristine CZTS@C-15 and (b,c) lithiated and delithiated CZTS@C-15.

Scheme 2. Schematic Diagram for the Lithium-Ion Storage Reaction Mechanism in CZTS@C

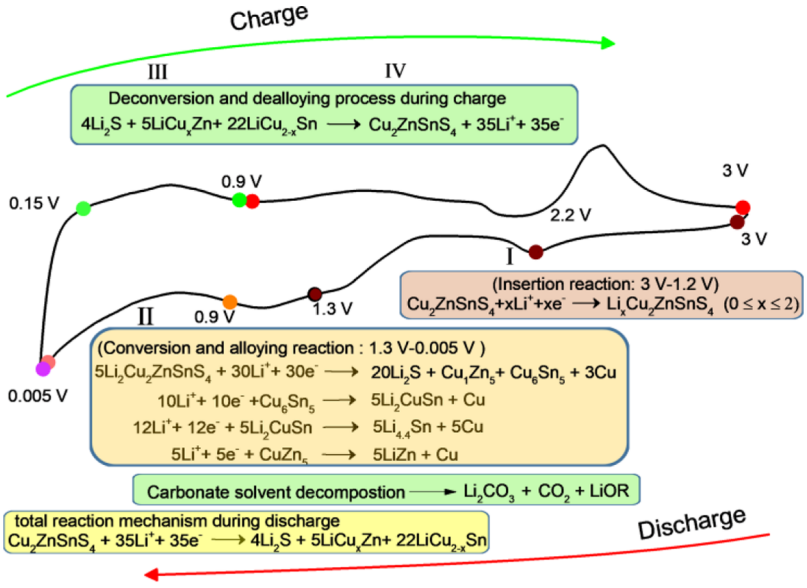

including alloys and Li_2S after 50 cycles (Figure S10). The XRD results suggest that the reaction mechanism of CZTS@C is similar after cycling.

High-resolution XPS measurements were carried out to determine the valence states of the elements in CZTS@C, as well as to confirm the lithium storage mechanism proposed on the basis of the *in situ* XRD data. Figure 9a shows the Cu 2p, Zn 2p, Sn 3d, and S 2p XPS peaks of CZTS@C. The high-resolution XPS spectra reveal that the CZTS sample contains Cu^+, Zn^{2+}, and Sn^{4+} states, which are consistent with the previous studies.[43,44] XPS spectra of CZTS@C-15 show the formation of Cu^+/Cu^0, Zn^{2+}/Zn^0, and Sn^{4+}/Sn^0 after the lithiation process, suggesting that metal alloy species are formed after many charge/discharge processes (Figure 9b).[14,43,45] Moreover, the binding energy in the sulfur spectrum shifts from 162 to 160 eV, which is attributed to the formation of Li_2S.[46] After the delithiation process, XPS results of CZTS@C-15 show that the oxidation state of Cu, Zn, and Sn increases, which corresponds to the formation of CZTS (Figure 9c). Thus, the XPS results are in a good agreement with XRD measurements. We next examine the effect of carbon coating on the SEI composition. Li 1s, O 1s, and F 1s XPS results show that Li_2CO_3, Li_2O, and LiF are the main products in the SEI layer (Figure S11).[46,47] Previous

https://doi.org/10.1021/acsomega.1c05076
ACS Omega 2022, 7, 9152−9163

studies suggest that LiF is beneficial for the stable SEI layer. However, XPS results of CZTS@C-15 and CZTS show that LiF is formed on both CZTS@C-15 and CZTS materials. The SEI layer of CZTS@C-15 exhibits a Li_2CO_3−rich layer, which could be beneficial for enhancing the ionic conductivity of the SEI layer in subsequent cycles, and thereby it results in good stability and rate capability.[46,48,49] The EIS results of CZTS and CZTS@C-15 show that the ionic conductivity of the SEI is improved on the CZTS@C-15 material (Figure S12 and Table S5).

The possible reasons for the CZTS@C nanostructure with higher areal capacity and improved electrochemical performance are discussed. First, the electronic conductivity of the electrode is improved. Second, the carbon layer can protect the CZTS electrode from the electrolyte. The side reaction could be suppressed and stable SEI can be formed. Third, carbon coating could act as a superior conducting medium for Li-ion migration and improve the stability performance even at a high current rate.[52,53]

Reaction Mechanism of CZTS@C. Previous studies suggested that the CZTS can be converted into Cu, $Li_{1.5}Zn$, $Li_{4.4}Sn$, and Li_2S during the lithiation process.[12] The discharge capacity of CZTS is over 1100 mA h/g[12,16] and high discharge capacity (~950 mA h/g) can be even achieved after 500 cycles.[50,51] Thus, the detailed mechanism is not fully understood yet. Because the CV results of these CZTS materials show different redox features, the CZTS materials synthesized by different methods could exhibit different chemical formulas and electrochemical behaviors. In the present study, the reaction mechanism of CZTS was examined using the *in situ* XRD measurement. Scheme 2 shows that the CZTS@C electrode underwent a multistep lithiation process through insertion, conversion, and alloying reactions, leading to a Li_xCZTS/Li_2S mixture and Cu−Sn/Zn alloy as intermediate phases. The XRD results shows the formation of Li_xCZTS, suggesting that the insertion process takes place at the initial stage. At the second stage, Li_2S and various alloys, including Cu−Zn/Cu−Sn, are formed during the alloying and conversion processes. These alloys can store the lithium through an insertion process below 1 V. Finally, the CZTS can be reformed during the delithiation process. Because the formation of various products suggests that the multielectron-transfer process takes place during cycling, we propose that CZTS can accommodate 35 Li ions, which results in a theoretical capacity of more than 2000 mA h/g. The detailed reactions are shown in the Supporting Information. We should note that other products with amorphous features or small quantity could not be observed by using XRD. The formation of these products could also show the multistep electron-transfer process. Thus, the theoretical gravimetric capacity of CZTS could be even higher. The CZTS material with uniform carbon coating allows rapid lithium ion and electron transport, leading to a high lithium storage capacity and improved stability of CZTS at high current rates.

CONCLUSIONS

We prepared carbon-coated CZTS nanoflowers with a 3D architecture by a simple and cost-effective solvothermal method. The electrochemical performance of the CZTS@C samples shows high gravimetric (1366 mA h/g) and areal (2.45 mA h/cm^2) capacities. Moreover, the CZTS@C-15 sample exhibits a highly stable behavior over 100 cycles even at high current rates. *In situ* XRD results reveals that CZTS undergoes the insertion process at the initial stage, followed by the alloying reaction and conversion reaction, which take place at around 1 V. The crystallinity of CZTS can be further improved after cycling. The CZTS nanoflower structure with an optimum amount of amorphous carbon shows improved electronic/ionic conductivity and lithium-ion diffusivity of the CZTS electrode material, which open up new opportunities for developing high-performance anode materials with high rate capability.

EXPERIMENTAL SECTION

Preparation of CZTS@C. The CZTS@C samples were prepared by a two-step process. First, 2 mM copper (II) acetate dehydrate [$Cu(OAc)_2{\cdot}xH_2O$], 1 mM zinc (II) acetate [$Zn(OAc)_2$], 1 mM tin (IV) chloride ($SnCl_4$), and 5 mM thiourea (CH_4N_2S) were dissolved in 70 mL of ethylene glycol. After constant stirring for 30 min, the transparent homogeneous mixture was transferred into a Teflon-lined stainless-steel autoclave and heated at 180 °C for 12 h, followed by natural cooling to room temperature. The obtained CZTS nanoflowers were collected by centrifugation, washed three times with deionized (DI) water and ethanol, and then dried under vacuum at 70 °C overnight. Then, different amounts (5−20 wt %) of glucose were mixed with the CZTS nanoflower powder in a 1:1 DI water−ethanol mixture solvent and dried at 70 °C under vacuum overnight. Finally, the as-prepared samples were annealed at 100 °C for 1 h, followed by 400 °C annealing for another hour at a heating rate of 10 °C/min under a nitrogen atmosphere, to obtain different carbon coating thicknesses over the CZTS surface. The as-prepared CZTS nanoflowers and the 5, 7, 10, 15, and 20 wt % carbon-coated CTZS samples were denoted as CZTS, CZTS@C-5, CZTS@C-7, CZTS@C-10, CZTS@C-15, and CZTS@C-20, respectively. The tap density of the CZTS-based materials is 2.5−3 g/cm^3.

Materials Characterization. The structural properties of the CZTS and CZTS@C samples before and after cycling were analyzed by XRD using a Bruker D2 diffractometer with Cu Kα radiation. The surface morphology of the samples was investigated using FE-SEM (JSM-6500). The microstructure, elemental distribution, and carbon coating thickness of the CZTS@C samples were analyzed using a high-resolution transmission electron microscope (JEOL2000FX), together with an FEI Tecnai G2 electron microscope coupled to an energy-dispersive X-ray spectrometer (Bruker AXS). To analyze the elemental composition and oxidation state of the carbon-coated CZTS samples, XPS measurements were performed with a monochromatic Al Kα source (1486.6 eV) operated under ultrahigh vacuum. The peak positions of the obtained XPS spectra were calibrated with respect to the C 1s peak position. Finally, all spectra were analyzed by the XPSPEAKS41 software. EA was carried out to determine the carbon content of the CZTS@C samples. The Raman spectra of the CZTS and CZTS@C samples were measured by a Horiba Jobin Yvon UV800 spectrometer with a 633 nm He−Ne laser as the excitation source.

Electrochemical Measurements. Coin-type 2032 cells were assembled in an argon-filled glovebox (LABstar, MBRAUN, Germany). The water and oxygen levels in the glovebox were less than 1 ppm. Metallic lithium (99.90%, Sigma-Aldrich) was used as the counter as well as reference electrodes, while Celgard 2325 was employed as the separator. The electrolyte used in the present work was 1 M $LiPF_6$ in a

https://doi.org/10.1021/acsomega.1c05076
ACS Omega 2022, 7, 9152−9163

mixture of ethylene carbonate, dimethyl carbonate (DMC), and ethylmethylcarbonate with 1% vinyl carbonate (1:1:1 weight ratio, LP-30, Merck, Germany). To prepare the working electrodes, the active materials, super-P carbon black, and poly(vinylidene fluoride) (Kynar 2801) binder were added in a mass ratio of 75:15:10 in *N*-methyl-2-pyrrolidone (NMP) solvent and stirred overnight to form a homogeneous slurry. The resulting paste was coated onto Cu foil and then dried at 70 °C for 12 h under vacuum. The loading amount of active materials was in the range of 1−2.3 mg/cm^2. Electrochemical performance measurements were conducted by galvanostatic charge/discharge tests performed in the potential range of 5 mV−3 V. Cyclic voltammetry (CV) measurements were carried out using a Solatron analytical 1470E cell test system, in the potential range of 0.005−3 V at a scan rate of 0.2 mV/s. EIS measurements of CZTS-Li metal cells were performed using a PARSTAT MC multichannel electrochemical workstation (Solatron analytical 1470E cell test system) in the frequency range from 1 MHz to 0.01 Hz. In all cells, the discharge capacity was calculated based on the mass of the active material, including CZTS and carbon. After cycling, the cells were disassembled in an argon-filled glovebox and the CZTS electrodes were rinsed with a DMC solution to remove residual salts for further characterization.

■ ASSOCIATED CONTENT

Supporting Information

The Supporting Information is available free of charge at https://pubs.acs.org/doi/10.1021/acsomega.1c05076.

Elemental analysis of CZTS@C samples with different carbon contents, XRD patterns of CZTS, Li_2S, Cu_6Sn_5, $CuZn_5$, and $Li_{22}Sn_5$, particle size of CZTS and CZTS@C with different carbon contents, charge and discharge curves of CZTS@C, cyclic performance of CZTS@C with different carbon contents, CE of pure CZTS and CZTS coated with different carbon contents, cyclic performance of CZTS@C-15 at a high current rate of 5000 mA/g, comparison of the electrochemical performance of present CZTS@C and various CZTS anode materials in LIB applications, voltage profiles and cyclic performance of CZTS@C-15/NMC532 in the full cell, FE-SEM images of CZTS and CZTS@C-15 after 100 cycles, calculated particle sizes of CZTS and Li_2S phases, XRD spectra of CZTS@C-15 during the lithiation process, *ex situ* XRD spectra of CZTS@C-15 after 50 cycles, *ex situ* XPS spectra F 1s, Li 1s, and O 1s of CZTS@C-15 and CZTS, Nyquist plots of CZTS@C coated with different amounts of carbon after 100 cycles, and fitted values of equivalent circuit parameters of CZTS and CZTS@C-15 (PDF)

■ AUTHOR INFORMATION

Corresponding Authors

Chih-Hao Lee − *Department of Engineering and System Science, National Tsing Hua University, Hsinchu 30013, Taiwan;* orcid.org/0000-0002-3898-6421; Email: chlee@mx.nthu.edu.tw

Heng-Liang Wu − *Center for Condensed Matter Sciences and Center of Atomic Initiative for New Materials, National Taiwan University, Taipei 10617, Taiwan;* orcid.org/0000-0003-1250-9851; Email: hengliangwu@ntu.edu.tw

Kuei-Hsien Chen − *Institute of Atomic and Molecular Sciences, Academia Sinica, Taipei 10617, Taiwan; Center for Condensed Matter Sciences, National Taiwan University, Taipei 10617, Taiwan;* orcid.org/0000-0002-9397-2516; Email: chenkh@pub.iams.sinica.edu.tw

Authors

Boya Venugopal − *Institute of Atomic and Molecular Sciences, Academia Sinica, Taipei 10617, Taiwan; Nanoscience and Technology Program, Taiwan International Graduate Program, Academia Sinica, Taipei 11529, Taiwan; Department of Engineering and System Science, National Tsing Hua University, Hsinchu 30013, Taiwan*

Zeru Syum − *Institute of Atomic and Molecular Sciences, Academia Sinica, Taipei 10617, Taiwan*

Sheng-Yu Yu − *Center for Condensed Matter Sciences, National Taiwan University, Taipei 10617, Taiwan;* orcid.org/0000-0002-7003-608X

Amr sabbah − *Institute of Atomic and Molecular Sciences, Academia Sinica, Taipei 10617, Taiwan*

Indrajit Shown − *Institute of Atomic and Molecular Sciences, Academia Sinica, Taipei 10617, Taiwan; Department of Chemistry, Hindustan Institute of Technology and Science, Chennai 603103, India*

Chih-Wei Chu − *Research Center for Applied Sciences, Academia Sinica, Taipei 11529, Taiwan;* orcid.org/0000-0003-0979-1729

Li-Chyong Chen − *Center for Condensed Matter Sciences and Center of Atomic Initiative for New Materials, National Taiwan University, Taipei 10617, Taiwan*

Complete contact information is available at: https://pubs.acs.org/10.1021/acsomega.1c05076

Notes

The authors declare no competing financial interest.

■ ACKNOWLEDGMENTS

The authors are thankful to Shashank Reddy for SEM measurements at Institute of Chemistry, Academia Sinica. The authors thank the Ministry of Science and Technology (MOST 109-2124-M-001-004 and MOST 110-2124-M-001-001), Academia Sinica, National Taiwan University, and the Ministry of Education (MOE) of Taiwan for financial support. A joint project between Academia Sinica and the Industrial Technology Research Institute (ITRI) and technical support from the Nano Core Facility of Academia Sinica (Taiwan) are also acknowledged.

■ REFERENCES

(1) Zhang, J.; Huang, T.; Liu, Z.; Yu, A. Mesoporous Fe_2O_3 nanoparticles as high performance anode materials for lithium-ion batteries. *Electrochem. Commun.* **2013**, *29*, 17−20.

(2) Shah, R.; Alam, N.; Razzaq, A. A.; Cheng, Y.; Yujie, C.; Jiapeng, H.; Xiaohui, Z.; Yang, P.; Zhao, D. Effect of Binder Conformity on the Electrochemical Behavior of Graphite Anodes with Different Particle Shapes. *Acta Phys.-Chim. Sin.* **2019**, *35*, 1382−1390.

(3) Zhou, X.; Wan, L.-J.; Guo, Y.-G. Binding SnO_2 nanocrystals in nitrogen-doped graphene sheets as anode materials for lithium-ion batteries. *Adv. Mater.* **2013**, *25*, 2152−2157.

(4) Syum, Z.; Venugopal, B.; Sabbah, A.; Billo, T.; Chou, T.-C.; Wu, H.-L.; Chen, L.-C.; Chen, K.-H. Superior lithium-ion storage performance of hierarchical tin disulfide and carbon nanotube-carbon cloth composites. *J. Power Sources* **2021**, *482*, 228923.

(5) Zhou, X.; Dai, Z.; Liu, S.; Bao, J.; Guo, Y.-G. Ultra-uniform SnOx/carbon nanohybrids toward advanced lithium-ion battery anodes. *Adv. Mater.* **2014**, *26*, 3943−3949.
(6) Venugopal, B.; Shown, I.; Samireddi, S.; Syum, Z.; Krishnamoorthy, V.; Wu, H.-L.; Chu, C.-W.; Lee, C.-H.; Chen, L.-C.; Chen, K.-H. Microstructural intra-granular cracking in Cu2ZnSnS4@C thin film anode enhanced the electrochemical performance in lithium-ion battery applications. *Mater. Adv.* **2021**, *2*, 5672.
(7) Sun, W.; Hu, Z.; Wang, C.; Tao, Z.; Chou, S.-L.; Kang, Y.-M.; Liu, H.-K. Effects of Carbon Content on the Electrochemical Performances of MoS_2-C Nanocomposites for Li-Ion Batteries. *ACS Appl. Mater. Interfaces* **2016**, *8*, 22168−22174.
(8) Syum, Z.; Billo, T.; Sabbah, A.; Venugopal, B.; Yu, S.-Y.; Fu, F.-Y.; Wu, H.-L.; Chen, L.-C.; Chen, K.-H. Copper Zinc Tin Sulfide Anode Materials for Lithium-Ion Batteries at Low Temperature. *ACS Sustainable Chem. Eng.* **2021**, *9*, 8970−8979.
(9) Wang, Y.; Zhang, X.; Chen, P.; Liao, H.; Cheng, S. In situ preparation of CuS cathode with unique stability and high rate performance for lithium ion batteries. *Electrochim. Acta* **2012**, *80*, 264−268.
(10) Weng, W.; Xu, J.; Lai, C.; Xu, Z.; Du, Y.; Lin, J.; Zhou, X. Uniform yolk−shell Fe_7S_8@ C nanoboxes as a general host material for the efficient storage of alkali metal ions. *J. Alloys Compd.* **2020**, *817*, 152732.
(11) Lin, J.; Lim, J.-M.; Youn, D. H.; Kawashima, K.; Kim, J.-H.; Liu, Y.; Guo, H.; Henkelman, G.; Heller, A.; Mullins, C. B. Self-Assembled Cu-Sn-S Nanotubes with High (De)Lithiation Performance. *ACS Nano* **2017**, *11*, 10347−10356.
(12) Yin, X.; Tang, C.; Chen, M.; Adams, S.; Wang, H.; Gong, H. Hierarchical porous Cu_2ZnSnS_4 films for high-capacity reversible lithium storage applications. *J. Mater. Chem. A* **2013**, *1*, 7927−7932.
(13) Bree, G.; Geaney, H.; Stokes, K.; Ryan, K. M. Aligned Copper Zinc Tin Sulfide Nanorods as Lithium-Ion Battery Anodes with High Specific Capacities. *J. Phys. Chem. C* **2018**, *122*, 20090−20098.
(14) Chiu, J.-M.; Chou, T.-C.; Wong, D. P.; Lin, Y.-R.; Shen, C.-A.; Hy, S.; Hwang, B.-J.; Tai, Y.; Wu, H.-L.; Chen, L.-C.; Chen, K.-H. A synergistic "cascade" effect in copper zinc tin sulfide nanowalls for highly stable and efficient lithium ion storage. *Nano Energy* **2018**, *44*, 438−446.
(15) Yang, X.; Xu, J.; Xi, L.; Yao, Y.; Yang, Q.; Chung, C. Y.; Lee, C.-S. Microwave-assisted synthesis of Cu_2ZnSnS_4 nanocrystals as a novel anode material for lithium ion battery. *J. Nanopart. Res.* **2012**, *14*, 931.
(16) Jiang, Q.; Chen, X.; Gao, H.; Feng, C.; Guo, Z. Synthesis of Cu_2ZnSnS_4 as novel anode material for lithium-ion battery. *Electrochim. Acta* **2016**, *190*, 703−712.
(17) Lin, J.; Guo, J.; Liu, C.; Guo, H. Three-Dimensional Cu_2ZnSnS_4 Films with Modified Surface for Thin-Film Lithium-Ion Batteries. *ACS Appl. Mater. Interfaces* **2015**, *7*, 17311−17317.
(18) Ponrouch, A.; Goñi, A. R.; Sougrati, M. T.; Ati, M.; Tarascon, J.-M.; Nava-Avendaño, J.; Palacín, M. R. A new room temperature and solvent free carbon coating procedure for battery electrode materials. *Energy Environ. Sci.* **2013**, *6*, 3363−3371.
(19) Ahmed, S.; Reuter, K. B.; Gunawan, O.; Guo, L.; Romankiw, L. T.; Deligianni, H. A High Efficiency Electrodeposited Cu_2ZnSnS_4 Solar Cell. *Adv. Energy Mater.* **2012**, *2*, 253−259.
(20) Camara, S. M.; Wang, L.; Zhang, X. Easy hydrothermal preparation of Cu_2ZnSnS_4 (CZTS) nanoparticles for solar cell application. *Nanotechnology* **2013**, *24*, 495401.
(21) Wang, K.; Shin, B.; Reuter, K. B.; Todorov, T.; Mitzi, D. B.; Guha, S. Structural and elemental characterization of high efficiency Cu_2ZnSnS_4 solar cells. *Appl. Phys. Lett.* **2011**, *98*, 051912.
(22) Zubair Ansari, M.; Khare, N. Thermally activated band conduction and variable range hopping conduction in Cu_2ZnSnS_4 thin films. *J. Appl. Phys.* **2015**, *117*, 025706.
(23) Gao, Q.; Qu, F.; Zheng, W.; Lin, H. A simple method to synthesize graphitic mesoporous carbon materials with different structures. *J. Porous Mater.* **2013**, *20*, 983−988.
(24) Rao, R.; Podila, R.; Tsuchikawa, R.; Katoch, J.; Tishler, D.; Rao, A. M.; Ishigami, M. Effects of layer stacking on the combination Raman modes in graphene. *ACS Nano* **2011**, *5*, 1594−1599.
(25) Brar, V. W.; Samsonidze, G. G.; Dresselhaus, M. S.; Dresselhaus, G.; Saito, R.; Swan, A. K.; Ünlü, M. S.; Goldberg, B. B.; Souza Filho, A. G.; Jorio, A. Second-order harmonic and combination modes in graphite, single-wall carbon nanotube bundles, and isolated single-wall carbon nanotubes. *Phys. Rev. B* **2002**, *66*, 155418.
(26) Ge, X.; Liu, S.; Qiao, M.; Du, Y.; Li, Y.; Bao, J.; Zhou, X. Enabling Superior Electrochemical Properties for Highly Efficient Potassium Storage by Impregnating Ultrafine Sb Nanocrystals within Nanochannel-Containing Carbon Nanofibers. *Angew. Chem., Int. Ed.* **2019**, *131*, 14720−14725.
(27) Zhang, Z.; Du, Y.; Wang, Q. C.; Xu, J.; Zhou, Y. N.; Bao, J.; Shen, J.; Zhou, X. A Yolk−Shell-Structured $FePO_4$ Cathode for High-Rate and Long-Cycling Sodium-Ion Batteries. *Angew. Chem., Int. Ed.* **2020**, *59*, 17504−17510.
(28) Liu, N.; Lu, Z.; Zhao, J.; McDowell, M. T.; Lee, H.-W.; Zhao, W.; Cui, Y. A pomegranate-inspired nanoscale design for large-volume-change lithium battery anodes. *Nat. Nanotechnol.* **2014**, *9*, 187−192.
(29) Yang, J.; Wang, Y.; Li, W.; Wang, L.; Fan, Y.; Jiang, W.; Luo, W.; Wang, Y.; Kong, B.; Selomulya, C.; Liu, H. K.; Dou, S. X.; Zhao, D. Amorphous TiO_2 Shells: A Vital Elastic Buffering Layer on Silicon Nanoparticles for High-Performance and Safe Lithium Storage. *Adv. Mater.* **2017**, *29*, 1700523.
(30) Vrankovic, D.; Graczyk-Zajac, M.; Kalcher, C.; Rohrer, J.; Becker, M.; Stabler, C.; Trykowski, G.; Albe, K.; Riedel, R. Highly Porous Silicon Embedded in a Ceramic Matrix: A Stable High-Capacity Electrode for Li-Ion Batteries. *ACS Nano* **2017**, *11*, 11409−11416.
(31) Qu, B.; Li, H.; Zhang, M.; Mei, L.; Chen, L.; Wang, Y.; Li, Q.; Wang, T. Ternary Cu_2SnS_3 cabbage-like nanostructures: large-scale synthesis and their application in Li-ion batteries with superior reversible capacity. *Nanoscale* **2011**, *3*, 4389−4393.
(32) Wan, H.; Peng, G.; Yao, X.; Yang, J.; Cui, P.; Xu, X. Cu_2ZnSnS_4/graphene nanocomposites for ultrafast, long life all-solid-state lithium batteries using lithium metal anode. *Energy Storage Mater.* **2016**, *4*, 59−65.
(33) Han, F.; Li, W.-C.; Li, D.; Lu, A.-H. In situ electrochemical generation of mesostructured Cu_2S/C composite for enhanced lithium storage: mechanism and material properties. *ChemElectroChem* **2014**, *1*, 733−740.
(34) Jang, Y. S.; Kang, Y. C. Facile one-pot synthesis of spherical zinc sulfide-carbon nanocomposite powders with superior electrochemical properties as anode materials for Li-ion batteries. *Phys. Chem. Chem. Phys.* **2013**, *15*, 16437−16441.
(35) Kim, T.-J.; Kim, C.; Son, D.; Choi, M.; Park, B. Novel SnS_2-nanosheet anodes for lithium-ion batteries. *J. Power Sources* **2007**, *167*, 529−535.
(36) Feng, J. K.; Lai, M. O.; Lu, L. Zn_2GeO_4 Nanorods synthesized by low-temperature hydrothermal growth for high-capacity anode of lithium battery. *Electrochem. Commun.* **2011**, *13*, 287−289.
(37) Lin, J.; Lim, J.-M.; Youn, D. H.; Liu, Y.; Cai, Y.; Kawashima, K.; Kim, J.-H.; Peng, D.-L.; Guo, H.; Henkelman, G.; Heller, A.; Mullins, C. B. Cu_4SnS_4-Rich nanomaterials for thin-film lithium batteries with enhanced conversion reaction. *ACS Nano* **2019**, *13*, 10671−10681.
(38) Varzi, A.; Mattarozzi, L.; Cattarin, S.; Guerriero, P.; Passerini, S. 3D Porous Cu-Zn Alloys as Alternative Anode Materials for Li-Ion Batteries with Superior Low T Performance. *Adv. Energy Mater.* **2018**, *8*, 1701706.
(39) Yang, Y.; Kang, X.; Huang, L.; Pan, D. Tuning the Band Gap of Cu2ZnSn(S,Se)4 Thin Films via Lithium Alloying. *ACS Appl. Mater. Interfaces* **2016**, *8*, 5308−5313.
(40) Lafond, A.; Guillot-Deudon, C.; Vidal, J.; Paris, M.; La, C.; Jobic, S. Substitution of Li for Cu in Cu2ZnSnS4: Toward Wide Band Gap Absorbers with Low Cation Disorder for Thin Film Solar Cells. *Inorg. Chem.* **2017**, *56*, 2712−2721.

https://doi.org/10.1021/acsomega.1c05076
ACS Omega 2022, 7, 9152−9163

(41) Wu, F.; Magasinski, A.; Yushin, G. Nanoporous Li_2S and MWCNT-linked Li_2S powder cathodes for lithium-sulfur and lithium-ion battery chemistries. *J. Mater. Chem. A* **2014**, *2*, 6064−6070.
(42) Su, L.; Fu, J.; Zhang, P.; Wang, L.; Wang, Y.; Ren, M. Uniform core−shell Cu_6Sn_5@C nanospheres with controllable synthesis and excellent lithium storage performances. *RSC Adv.* **2017**, *7*, 28399−28406.
(43) Ma, T.; Yu, X.; Li, H.; Zhang, W.; Cheng, X.; Zhu, W.; Qiu, X. High volumetric capacity of hollow structured SnO_2@ Si nanospheres for lithium-ion batteries. *Nano Lett.* **2017**, *17*, 3959−3964.
(44) Hwa, Y.; Kim, W.-S.; Yu, B.-C.; Kim, H.; Hong, S.-H.; Sohn, H.-J. Reversible storage of Li-ion in nano-Si/SnO_2 core−shell nanostructured electrode. *J. Mater. Chem. A* **2013**, *1*, 3733−3738.
(45) Baggetto, L.; Ganesh, P.; Meisner, R. P.; Unocic, R. R.; Jumas, J.-C.; Bridges, C. A.; Veith, G. M. Characterization of sodium ion electrochemical reaction with tin anodes: Experiment and theory. *J. Power Sources* **2013**, *234*, 48−59.
(46) Li, Z.; Zhang, S.; Zhang, C.; Ueno, K.; Yasuda, T.; Tatara, R.; Dokko, K.; Watanabe, M. One-pot pyrolysis of lithium sulfate and graphene nanoplatelet aggregates: in situ formed Li_2S/graphene composite for lithium−sulfur batteries. *Nanoscale* **2015**, *7*, 14385−14392.
(47) Wu, B.; Ren, Y.; Mu, D.; Liu, X.; Wu, F. Electrochemical performance of 5 V $LiNi_{0.5}Mn_{1.5}O_4$ cathode modified with lithium carbonate addition in electrolyte. *J. Power Sources* **2014**, *272*, 183−189.
(48) Yao, K. P. C.; Kwabi, D. G.; Quinlan, R. A.; Mansour, A. N.; Grimaud, A.; Lee, Y.-L.; Lu, Y.-C.; Shao-Horn, Y. Thermal Stability of Li_2O_2 and Li_2O for Li-Air Batteries: In Situ XRD and XPS Studies. *J. Electrochem. Soc.* **2013**, *160*, A824−A831.
(49) Wu, B.; Ren, Y.; Mu, D.; Liu, X.; Yang, G.; Wu, F. Effect of lithium carbonate precipitates on the electrochemical cycling stability of $LiCoO_2$ cathodes at a high voltage. *RSC Adv.* **2014**, *4*, 10196−10203.
(50) Dedryvère, R.; Laruelle, S.; Grugeon, S.; Poizot, P.; Gonbeau, D.; Tarascon, J. M. Contribution of X-ray Photoelectron Spectroscopy to the Study of the Electrochemical Reactivity of CoO toward Lithium. *Chem. Mater.* **2004**, *16*, 1056−1061.
(51) Lin, J.; Guo, J.; Liu, C.; Guo, H. Ultrahigh-performance Cu_2ZnSnS_4 thin film and its application in microscale thin-film lithium-ion battery: comparison with SnO_2. *ACS Appl. Mater. Interfaces* **2016**, *8*, 34372−34378.
(52) Cai, W.; Yan, C.; Yao, Y.-X.; Xu, L.; Xu, R.; Jiang, L.-L.; Huang, J.-Q.; Zhang, Q. Rapid Lithium Diffusion in Order@Disorder Pathways for Fast-Charging Graphite Anodes. *Small Struct.* **2020**, *1*, 2000010.
(53) Kong, L.; Tang, C.; Peng, H. J.; Huang, J. Q.; Zhang, Q. Advanced energy materials for flexible batteries in energy storage: A review. *Smart Mater.* **2020**, e1007.

https://doi.org/10.1021/acsomega.1c05076
ACS Omega 2022, 7, 9152−9163